[1] Javad Naderifar

[2] Mostafa Khazaee

[32]Seyed H. Sadati

A Synergistic Fault-Tolerant Flight Control System based on Adaptive Neural Networks and an Enhanced Adaptive Super-Twisting Algorithm

JES Journal of Electrical Systems

Abstract: In This study introduces a sophisticated fault-tolerant flight control system designed to address the challenges of disturbance rejection and sensor fault compensation in aircraft systems, particularly under conditions of high angle of attack and severe noise. The proposed framework integrates an Adaptive Super-Twisting Observer (ASTO) with an Adaptive Neural Observer enhanced by an Extended Kalman Filter (ANO-EKF), complemented by a robust Backstepping control strategy that incorporates a smooth switching mechanism. A central innovation of this study lies in the development of the adaptive super-twisting observer, which improves estimation accuracy by dynamically adjusting observer gains according to system behavior. This approach significantly enhances disturbance rejection. The proposed method increases system robustness without requiring prior knowledge of disturbance bounds, ensuring superior adaptability in sensor noise and faults. To further enhance fault tolerance, the ANO-EKF is introduced, leveraging a neural network for adaptive state refinement, while the EKF ensures precise fault detection and compensation. This integrated approach guarantees reliable performance even under severe sensor faults. Additionally, a Backstepping-based control strategy is employed, incorporating a sigmoid-based smooth switching function to ensure seamless transitions between actual and estimated states, effectively reducing transient oscillations and minimizing control disruptions. Extensive nonlinear dynamic simulations using an F-18A fighter jet model highlight the enhanced effectiveness of the proposed approach in comparison with conventional methods. The outcomes indicate that incorporating ASTO into the Fault-Tolerant Control (FTC) framework enhances tracking accuracy by 48.3% and reduces chattering by 5.7%, underscoring its suitability for practical aerospace applications.

Keywords: Robust Fault-tolerant control; disturbance mitigation; adaptive neural observer; adaptive super twisting algorithm; backstepping control strategy.

I. INTRODUCTION

The disturbances and faults in control systems pose many challenges and attract a lot of research on non-linear systems to identify their effects [1].Researchers apply Sliding Mode Control (SMC) as a powerful method in several areas, including spacecraft management and hypersonic vehicle regulation, Methodologies of Sliding Mode Control (SMC) are frequently affected by two major constraints: rapid oscillations and semi-global convergence. To address the issue of rapid oscillations, higher-order sliding mode (HOSM) theories, especially second-order sliding modes (SOSM), have been widely advanced [2]. To minimize chattering, advanced SMC techniques and the second-order super twisting algorithm (STA) have been introduced [3]. Among these, the Super-Twisting Algorithm (STA) stands out as a prominent approach, offering finite-time convergence capabilities that conventional Sliding Mode Observers (SMOs) cannot achieve[4]. In addition, time-varying and adaptive sliding mode control strategies enhance the efficiency and address chattering [5]. The Adaptive Super Twisting Algorithm (ASTA) handles unknown disturbances, and the Super Twisting Observer (STO) compensates for measurement limitations and sensor noise and Furthermore, the adaptive mechanism dynamically adjusts the algorithm gains without inducing excessive conservatism, leading to enhanced tracking accuracy and reduced control effort. Such advancements contribute significantly to the resilience and performance of modern guidance and control systems in challenging operational environments [6]. ASTA and STO are successfully applied in fixed-wing UAV control and demonstrate their effectiveness [7]. The super-twisting algorithm provides continuous control, finite convergence time [8], and disturbance reaction without precise knowledge of disturbances [8-9]. In this study, to mitigate disturbances and benefit from all the mentioned advantages, an Adaptive Super-Twisting Observer (ASTO) is employed as a disturbance observer. To ensure reliable system operation and address errors from angular velocity sensors, it is crucial to consider disruptions and faults. Fault diagnosis involves tasks such as detection, isolation, and identification [10]. Analytical redundancy-based fault diagnosis is a cost-effective approach but faces challenges like noise, modeling errors, and system complexity. In this line, the synchronized observers and adaptive learning techniques provide fault detection and localization algorithms. The neural controllers with online error back-propagation training handle large errors [11]. Neural

[1] Faculty of Aerospace, Malek Ashtar University of Technology, Tehran, Iran

[2] *Corresponding author: Faculty of Aerospace, Malek Ashtar University of Technology, Tehran, Iran, khazaee_m@mut.ac.ir

[3] Faculty of Aerospace, Malek Ashtar University of Technology, Tehran, Iran

estimators aid identification through dynamic feedback with networks to localize the operational faults [12]. The Model Reference Adaptive Controller (MRAC) adapts to detect structural failures [13].The optimal and adaptive algorithm for the Kalman filter has been implemented in the lateral dynamics of the Boeing 747 aircraft to address a particular sensor failure [14].A resilient control system for autonomous drones has been developed to effectively manage sensor failures [15]. This system includes a methodology for identifying and isolating sensor malfunctions that impact the mean value of the Kalman Filter series. A flexible dual-stage KF algorithm differentiates and estimates sensor and actuator faults while assessing control performance and the degree of actuator failures. Another proactive fault-tolerant system utilizing Model Predictive Control (MPC) and an enhanced state KF is designed for a quadrotor with interval constraints to withstand diminished actuator efficiency [16]. Recent research has investigated the use of Integral Sliding Mode Strategy in nonlinear systems with uncertainties, aiming to reduce high-frequency oscillations and enhance transient performance. This paper introduces the adaptive super-twisting observer method as an effective tool for compensating matched disturbances and reducing high-frequency oscillations[17]. Based on the mentioned references, all the methods have primarily focused on separate fault and disturbance analysis, either in the domain of disturbance attenuation or the elimination of fault effects. This paper aims to investigate fault and disturbance simultaneously, considering limited convergence time and reducing chattering, through the utilization of a soft-switching control command. This paper presents an integrated approach that addresses both fault and disturbance effects, introducing an innovative fusion of an adaptive super-twisting algorithm (ASTA) and a robust observer. The adaptive mechanism dynamically adjusts algorithm gains to enhance robustness and minimize chattering, while a soft-switching mechanism ensures seamless transitions, setting this work apart from existing methods.The proposed resilient flight management system is designed to handle sensor faults, disturbances, and external interference effectively. Key contributions include:

1) Disturbance Rejection without Prior Knowledge: The ASTO observer utilize a self-adaptive mechanism to fine-tune system parameters dynamically. This minimizes energy consumption, mitigates chattering, and enhances disturbance rejection, ensuring improved system resilience and reduced control effort.

2) Accurate Sensor Output Estimation: Lost sensor outputs are accurately estimated using healthy sensors through an Enhanced and adaptive Super-Twisting Algorithm. This is achieved within the state estimation framework, offering reliable state reconstruction under sensor fault conditions.

3) Fault Detection and Mitigation: A self-adaptive neural network, coupled with an Extended Kalman Filtering technique, effectively detects and compensates for sensor faults. Additionally, a robust nonlinear backstepping control strategy with soft-switching actions, implemented using a sigmoid function, mitigates excessive control effort during faults, disturbances, and noise. This ensures the aircraft maintains stable, automatic flight under adverse conditions.

The proposed approach enhances aircraft safety, reliability, and operational efficiency, making it a robust solution for modern flight management systems.

II. GENERAL FORM OF SYSTEM DYNAMICS

To identify faults in a control system, having a precise dynamic model is essential. For high-speed maneuverable aircraft, the behavior can be effectively described using nonlinear differential equations, as referenced in sources [18 -20]. In Eq.1 illustrates this general problem.

$$\begin{aligned} \dot{x}(t) &= f(x(t)) + g(x(t))u(t) + \zeta(t,x) + E\psi(x) \\ y(t) &= h(x(t)) + f_s(x,u) + v \end{aligned} \qquad (1)$$

Let u $\in \mathbb{R}^m$ denote the input vector, **y** $\in \mathbb{R}^r$ represent the output vector, and x $\in \mathbb{R}^n$ be the state vector. The functions involved are, which describes the state dynamics $f: \mathbb{R}^n \to \mathbb{R}^n$ which defines the dynamics related to the inputs, and $g: \mathbb{R}^m \to \mathbb{R}^n$ which represents the output dynamics $h: \mathbb{R}^n \to \mathbb{R}^r$، The error vector $f_s(\mathrm{x}, \mathrm{u})$ accounts for sensor errors. The matrix E is a constant matrix with known values. The function $\zeta(t, \mathrm{x})$ is a specified nonlinear function, while $\psi(\mathrm{x})$ represents external disturbancer affecting the system. Additionally, v represents noise

III. ENHANCED ASTA ALGORITHM

Enhanced super Twisting Algorithm is derived based on the 2nd order sliding mode control to reduce chattering and provide smooth control. This approach is implemented as described in Eq.2 per [8].

$$\begin{cases}\dot{x}_1 = x_2 \\ \dot{x}_2 = F(t, x_1, x_2) + u_c + \psi(t,x) + \zeta(t,x)\end{cases} \quad (2)$$

Where x_1 and x_2 represent the system states, y denotes the output, $\Psi(t,x)$ represents the bounded external disturbance, $\zeta(t,x)$ represents the nonlinear term, and u_c is considered as a part of control input, The Super-twisting observer accurately estimates state variables in uncertain and disturbed systems. It doesn't need prior knowledge of disturbance bounds or high-frequency disturbances. The adaptive super-twisting algorithm reduces chattering and over-estimation of observer gains. The dynamics of the adaptive Super Twisting Observer (STO) are described by Eq. (3) as referenced by [8].

$$\begin{cases}\dot{x}_1 = x_2 \\ \dot{x}_2 = F^*(t, x_1, x_2, u) + \psi(t,x) + \zeta(t,x)\end{cases} \quad (3)$$

The super-twisting algorithm enables accurate state estimation for second-order system models, as described by Eq. (4) in reference [21].

$$\begin{cases}\dot{\hat{x}}_1 = \hat{x}_2 + \lambda|e|^{0.5}sign(e) \\ \dot{\hat{x}}_2 = F^*(t, x_1, x_2, u) + \psi(t,x) + \zeta(t,x) + asign(e)\end{cases} \quad (4)$$

by Defining $e_i = x_i - \hat{x}_i$,the observer error dynamics equation can be represented as Eq (5) while the function $F^*$is described in Eq (6) in reference [21].

$$\begin{aligned}\dot{e}_1 &= e_2 + \lambda|e|^{0.5}sign(e) \\ \dot{e}_2 &= f^*(t, \hat{x}_1, \hat{x}_2, u) + \psi(t,x) + \zeta(t,x) - asign(e)\end{aligned} \quad (5)$$

$$f^* \triangleq F^*(t, x_1, x_2, u) - F^*(t, \hat{x}_1, \hat{x}_2, u) + \psi(t, \hat{x}_1, \hat{x}_2, u) + \zeta(t, x_1, x_2, u)\&|f^*(t, \hat{x}_1, \hat{x}_2, u)| < f^+ \quad (6)$$

Considering the limitations on the states and control inputs, f^+ is regarded as the maximum bound of the function f^*, representing an unknown constant, Furthermore, ψ and ξ includes the disturbance term and nonlinear components in Equation (6). By choosing suitable observer gains lambda and alpha in Equation (4), it has been demonstrated that the error behavior tends towards zero.

Consequently resulting in $x_1 = \hat{x}_1$ and $x_2 = \hat{x}_2$ after a finite time $t \geq T_0$. Additionally, the current observer gains shown in Table 1 can be adaptively obtained as described by Equation (7) in [21].

$$\begin{aligned}\dot{\lambda} &= \begin{cases}k_1 sign(|e| - \varepsilon) & if\lambda > \alpha_m \\ k_2 & if\lambda \leq \alpha_m\end{cases} \\ \alpha &= k_3\lambda\end{aligned} \quad (7)$$

where k_1, k_2, k_3 and ε are non-negative constants, and α_m is a small positive constant chosen as necessary in reference[21].

The super-twisting observer accurately estimates the aircraft's angular velocity without direct measurement by using three measurable aircraft states (α,β,μ). These states correspond to the attack angle, sideslip angle, and rotation angle around the velocity vector. They are described by specific equations (Eq. 8, Eq. 9, and Eq. 10) when disturbances are present.

$$\begin{aligned}&\dot{x}_1 = x_2 and \dot{x}_2 = \dot{p} = F(t,x) + \psi(t,x) + \xi \\ &\dot{\hat{\mu}} = \hat{p} + \lambda_1|\mu - \hat{\mu}|^{0.5}sign(\mu - \hat{\mu}) \\ &\dot{\hat{p}} = F(t, \hat{x}_1, \hat{x}_2, u) + \alpha_1 sign(\mu - \hat{\mu}) + \psi(t,x) + \xi\end{aligned} \quad (8)$$

$$\begin{aligned}&\dot{x}_1 = x_2 and \dot{x}_2 = \dot{q} = f(t,x) + \psi(t,x) + \xi \\ &\dot{\hat{\alpha}} = \hat{q} + \lambda_2|\alpha - \hat{\alpha}|^{0.5}sign(\alpha - \hat{\alpha}) \\ &\dot{\hat{q}} = f(t, \hat{x}_1, \hat{x}_2, u) + \alpha_2 sign(\alpha - \hat{\alpha}) + \psi(t,x) + \xi\end{aligned} \quad (9)$$

$$\begin{aligned}&\dot{x}_1 = x_2 and \dot{x}_2 = \dot{r} = f(t,x) + \psi(t,x) + \xi \\ &\dot{\hat{\beta}} = \hat{r} + \lambda_3\left|\beta - \hat{\beta}\right|^{0.5}sign(\beta - \hat{\beta}) \\ &\dot{\hat{r}} = f(t, \hat{x}_1, \hat{x}_2, u) + \alpha_3 sign(\beta - \hat{\beta}) + \psi(t,x) + \xi\end{aligned} \quad (10)$$

For a system with a relative degree of two, the sliding surface is redefined as shown below by using the states estimated by the observer, ensuring stability in the control in Eq. (11).

$$\hat{S} = \lambda x_1 + \hat{x}_2 \qquad if\ \ \lambda > 0 \tag{11}$$

To implement the control law, where$F(t, \hat{x}_1, \hat{x}_2, u) = f(\hat{x}) + g(\hat{x})u = \dot{\hat{x}}_2$. The time derivative of equation (11) needs to be calculated In Eq. (12).

$$\dot{\hat{S}} = \lambda \dot{x}_1 + \dot{\hat{x}}_2 \tag{12}$$
$$\dot{\hat{S}} = \lambda x_2 + f(\hat{x}) + g(\hat{x})u + \alpha sign(e) + \psi(t,x) + \xi$$

By inserting $x_2 = e_2 + \hat{x}_2$into equation (12), it can be expressed in a different form In Eq. (13).

$$\dot{\hat{S}} = \lambda \hat{x}_2 + \lambda e_2 + f(\hat{x}) + g(\hat{x})u + \alpha sign(e) + \psi(t,x) + \xi \tag{13}$$

Additionally, demonstrates that to stabilize the closed-loop system, the term $-\alpha sign(e)$ needs to be included in the control input In Eq. (14).

$$u_{astc} = g_1(\hat{x})^{-1}(-\lambda \hat{x}_2 - \alpha sign(e) - k_1|\hat{s}|^{0.5} sign(\hat{s}) - k_2 \int_0^t sign(\hat{s}(\tau))\, d\tau - f_1(\hat{x})) \tag{14}$$

The controller gains k_1 and k_2 are chosen to exceed the highest expected level of disturbance, thereby ensuring that the disturbance is adequately mitigated by reference [8,21] The controller gains k_1 and k_2 can be determined using the following adaptive algorithm.where $\eta, \varepsilon, \mu, \gamma, \alpha$ and w_a are considered are arbitrary positive constands.

$$\dot{k}_1 = \begin{cases} w_a \sqrt{\frac{\gamma}{2}}\, sign(|\sigma| - \mu). & if\ k_1 > a_m \\ \eta & if k_1 > a_m \end{cases} \quad \& \ k_2 = 2\varepsilon k_1 \tag{14.1}$$

For a comparative analysis of the adaptive super-twisting approach (ASTO) and the Super-Twisting Observer (STO) regarding disturbance rejection and estimation accuracy, a diagram of the STO algorithm is shown in Fig. 1, with the observer tuning parameters provided in Table 1.

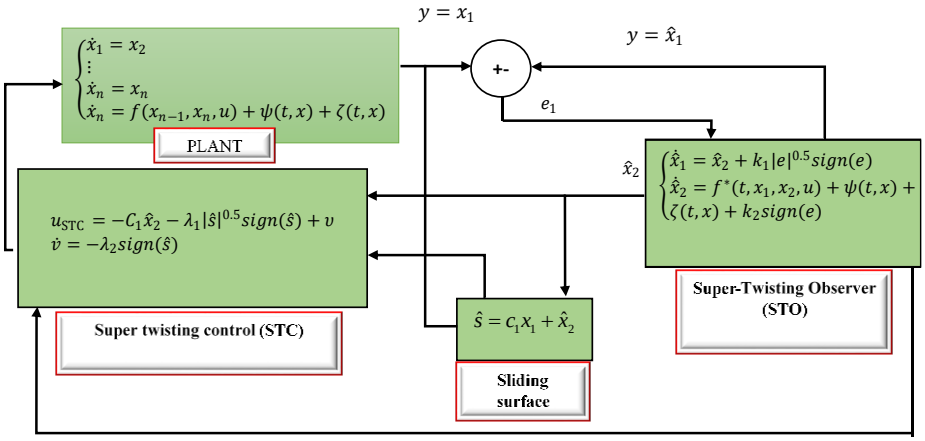

Fig.1. The general framework and flowchart of the control utilizing the Super-twisting Observer (STO)

Table 1. Parameter gains of control utilizing the adaptive Super-twisting Observer (ASTO) and the Super-Twisting Observer (STO).

λ	α_m	α	k_1	k_2	k_3	ASTO
10	3	2.35	4	2	0.18	Observer -1 (estimation -p)
5	3.5	2.60	3.5	1.9	0.18	Observer -2 (estimation- q)
6.2	3	1.60	3.75	2	0.18	Observer -2 (estimation- r)
λ_1	λ_2	k_1	k_2	STO		

STC		STO		gain values
0.5	1.5	10	1.35	Observer -1 (estimation -p)
0.5	1.6	9	1.60	Observer -2 (estimation- q)
0.5	1.2	8.5	1.60	Observer -2 (estimation- r)

To evaluate the two algorithms, the pitch angular velocity of the aircraft in Fig. 2 has been estimated using the two proposed algorithms. The performance items are presented in Table 2.

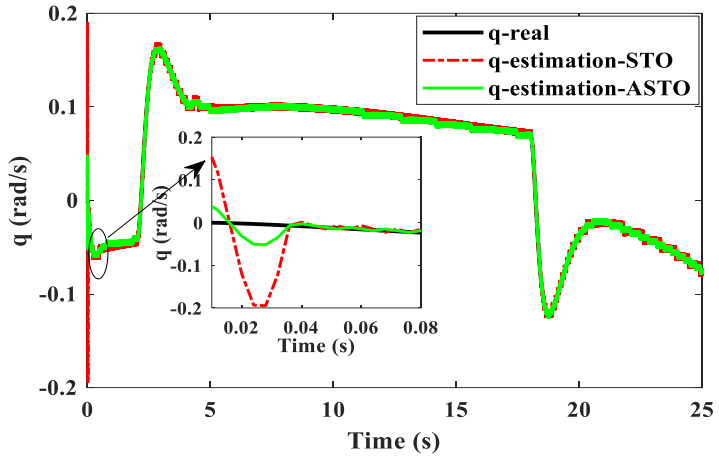

Fig. 2. Comparison of pitch angular velocity estimation ASTO versus STO.

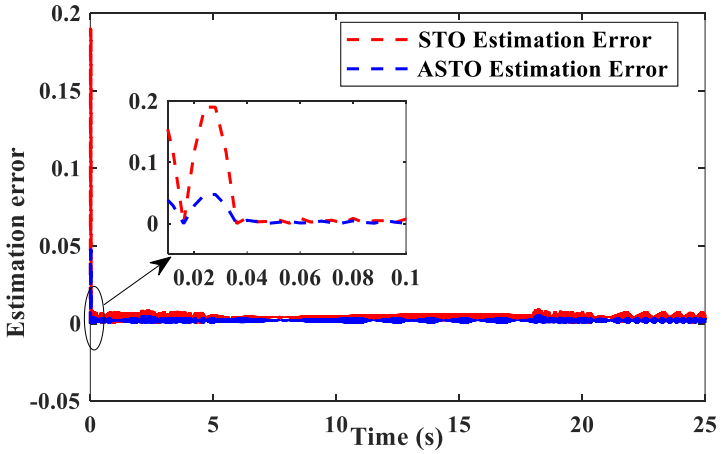

Fig. 3. Estimation error of pitch rates using the ASTO and STO algorithms

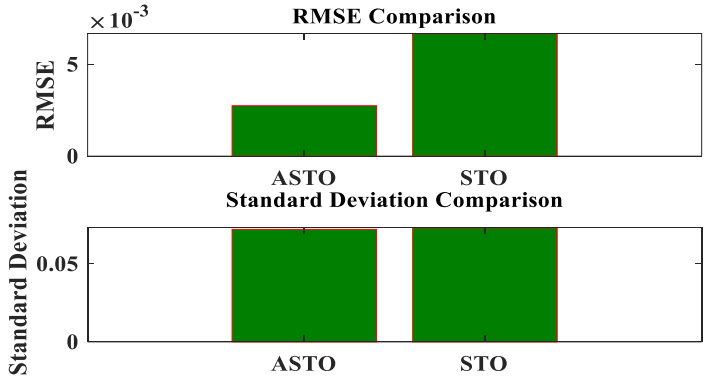

Fig. 4. Comparison of the RMSE (Root Mean Square Error) and standard deviation between the Adaptive Super-Twisting Observer (ASTO) and the conventional Super-Twisting Observer (STO).

Table 2. Performance index utilizing the adaptive Super-Twisting Observer (ASTO) and the conventional Super-Twisting Observer (STO).

Performance index	RMSE	Standard Deviation	Mean Valu
Angular velocity real	0.042285	0.072209	0.042285
Angular velocity estimation STO	0.0066653	0.073006	0.04274
Angular velocity estimation ASTO	0.0027447	0.072082	0.042078
Improvment	58.82	1.26%	1.55%

Given the superior performance of the adaptive super-twisting algorithm, the angular velocity in all three channels was calculated using ASTO method for the aircraft and is shown in Fig. 5.

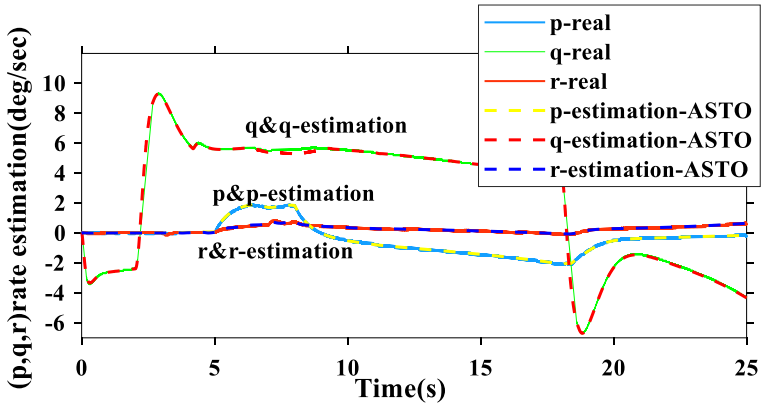

Fig. 5. Estimation of roll, pitch, and yaw angular velocities using an Adaptive Super-Twisting Observer

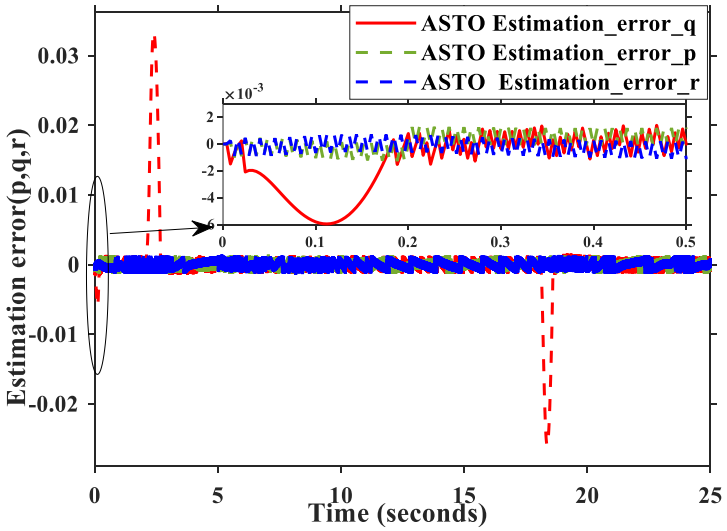

Fig. 6. Angular velocity estimation errors for roll, pitch, and yaw using the Adaptive Super-Twisting Observer

The comparative evaluation between the Adaptive Super-Twisting Observer (ASTO) and the traditional Super-Twisting Observer (STO) emphasizes the considerable benefits of the adaptive method for estimating angular velocities. ASTO consistently outperforms STO in important performance measures, such as Root Mean Square Error (RMSE), standard deviation, and accuracy of the average value. Notably, ASTO achieves a remarkable

58.82% reduction in RMSE, with a value of 0.0027 compared to 0.0067 for STO, reflecting its superior estimation accuracy.The adaptive gain tuning mechanism of ASTO effectively mitigates noise and disturbances, enhancing its robustness in real-world scenarios. Additionally, ASTO demonstrates a 1.26% reduction in standard deviation (0.0721 vs. 0.0730 for STO), ensuring greater stability and consistency in its estimates a crucial factor in Sensor noise . Its mean value accuracy further emphasizes this superiority, with ASTO achieving a 1.55% improvement by maintaining a closer alignment with the actual mean value (0.0421 vs. 0.0427 for STO).These results highlight the resilience and precision of ASTO, making it an ideal choice for advanced flight control systems operating under uncertain conditions. The adaptive control strategy employed by ASTO ensures reliable performance by dynamically adjusting parameters in response to system disturbances, reinforcing its value in safety-critical aerospace applications.

After eliminating disturbances using neural-adaptive and extended Kalman filter algorithms, the next step is to detect and isolate errors. Neural networks are utilized for this task, due to universal approximation for nonlinear Lipchitz functions. To ensure the analysis and stability assessment of the Neural Adaptive Observer (NAO), specific assumptions are considered.

Assumption 1: Each state variable x(t) is accessible for measurement.

Assumption 2: The function f(x(t)) and h(x(t)) are assumed to be differentiable with concerning the state vector: x: $(t) = \frac{\partial f}{\partial x}\Big|_{x=\hat{x}}$ and $C(t) = \frac{\partial h}{\partial x}\Big|_{x=\hat{x}}$

where A(t) is an n×n matrix and C(t) an n×r matrix. Therefore, the equation presented below can be derived from the expansion of f(x(t)) and h(x(t)) with respect to x̂:

$$\begin{cases} f(x) - f(\hat{x}) = A(t)\tilde{x}(t) + \varphi(\hat{x}, x) \\ h(x) - h(\hat{x}) = A(t)\tilde{x}(t) + \psi(\hat{x}, x) \end{cases} \quad (15)$$

where and ψ(x̂,x)=O(‖x̃(t)‖), which include the higher order terms of estimation error as follows:

$$\tilde{x}(t) = x(t) - \hat{x}(t) \quad (16)$$

Assumption 3: The error $f_s(x,u)$ is bounded by f_m.

Assumption 4: The real number $l_\varphi>0$ and $l_\psi>0$ exists, if φ and ψ is limited by the following relation: as Eq. (17).

$$\begin{cases} \|\varphi(x, \hat{x})\| \le l_\varphi \|\tilde{x}(t)\| \\ \|\psi(x, \hat{x})\| \le l_\psi \|\tilde{x}(t)\| \end{cases} \quad (17)$$

Assumption 5: The symmetric matrix Γ(t) satisfies condition $\beta_1 I_n \le \Gamma(t) \le \beta_2 I_n$ where β_1 and β_2 represent positive real value and Γ(t) denotes the outcome of the Lyapunov equation given by eq.(18).

$$A^T \Gamma(t) + \Gamma(t) A + \dot{\Gamma}(t) = -Q \quad (18)$$

where Q represents a symmetric matrix that is positive definite. The Neural Adaptive Observer is adjusted using the input from the EKF observer, denoted as M(t), allowing it to identify deviations caused by the error [22].

IV. NEURAL-ADAPTIVE OBSERVER

The observer in consideration is designed to estimate the error present within the nonlinear system defined by equation (1). It is constructed based on the system's input and output as outlined in equation (19).

$$\begin{aligned} \dot{\hat{x}} &= f(\hat{x}(t)) + g(\hat{x}(t))u(t) \\ \hat{y}(t) &= h(\hat{x}(t)) + M(t) \\ M_i(t) &= W_i(t)\sigma(V_i(t)I_i(t)) \end{aligned} \quad (19)$$

where x̂(t) is the observer's state vector at time t. $M_i(t)$ For component i=1,…,n, is the input vector of the observer M(t). $W_i(t)$ and $V_i(t) = \left[V_{i,1}(t), \cdots, V_{i,p+q}(t)\right]$ are the ith input parameters in the adaptive neural network at the time of t.

$$I_i(t) = [M_i(t-\tau), \cdots, M_i(t-p\tau), \tilde{y}_i(t-\tau), \cdots, \tilde{y}_i(t-p\tau)]^T \quad (20)$$

where τ denotes the sampling period or time step. The$\hat{y}_i(t) = h(x(t)) - h(\hat{x}(t))$ term refers to the estimated error component of the output. The σ(·) sigmoid activation function is chosen in this study $\sigma(x) = (1 - e^{-x})/(1 + e^{-x})$. The existence of large eigenvalue for p and q,While ensuring the convergence of the training process is important, it can lead to longer processing times and potential delays. The observer's input is updated iteratively, using previous outputs from the p observer, specifically M(k-τ) and M(k-pτ), along with the system's output error q, before updating ỹ(t-qτ), as detailed in reference [22].

V. UPDATING LAW AND ITS CONVERGENCE

The Extended Kalman Filter (EKF) method is utilized to adjust the coefficients of the adaptive neural system, ensuring fast convergence. Figure 7 depicts the steps involved in the EKF algorithm for updating these parameters. In this context, η_i denotes the training constant, $K_i(k)$ refers to the Kalman filter gain, $P_i(k)$ signifies the covariance matrix associated with the state estimation error, and $R_i(k)$ indicates the covariance matrix of the predicted measurement noise The matrix $R_i(k)$ is updated recursively as Fig. 7.

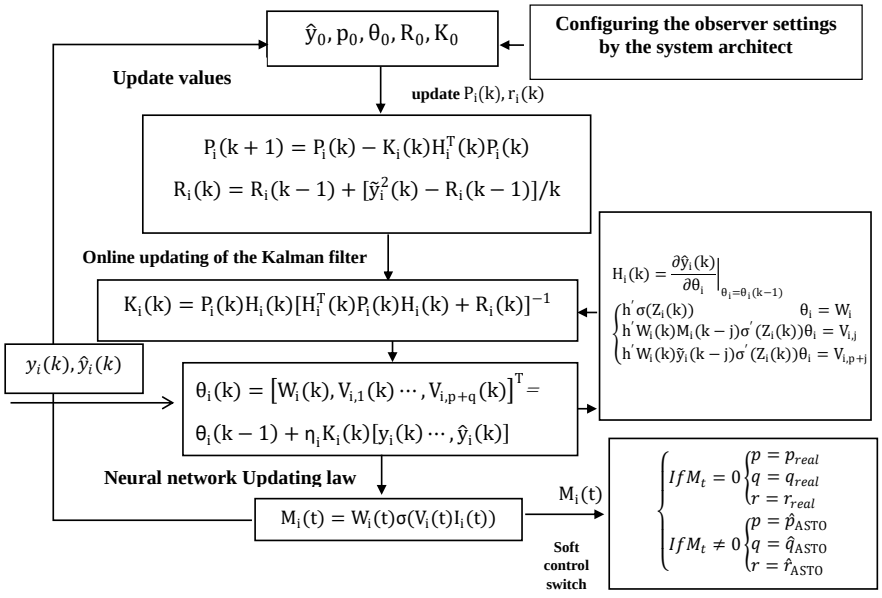

Fig. 7. Block diagram of neural network coefficient update using EKF in [22].

To ensure the convergence of the NAO weight updates using the EKF, the following assumption must be satisfied.

Assumption 6: The estimated noise variance, $R_i(k)$, as defined in Equation (21).

$$R_i(k) = R_i k - R_i + [e_i(k)^2 - R_i(k-1)]/k \tag{21}$$

must satisfy the following condition for proper convergence:

$$0 < R_i(k) << H_i(k)^T P_i(k) H_i(k) \tag{22}$$

Theorem 1: The adjustment of the NAO weights will reach convergence, provided that the learning parameter meets the following requirement:

$$0 < \eta_i < \frac{2R_i(K)}{\|H_i(K)\|\lambda_{max\,(P_i(K))}} + 2 \tag{23}$$

From Equations 22 and 23, it can be deduced that:

$$0 < \eta_i < 2 + \frac{2R_i}{H_i{}^T P_i H_i} = 2\frac{H_i{}^T p_i H_i + R_i}{H_i{}^T P_i H_i} \tag{24}$$

So

$$0 < \eta_i {H_i}^T P_i H_i \left[{H_i}^T P_i H_i + R_i \right]^{-1} < 2 \qquad (25)$$

From Equations 24 and 25, by defining $k_i(t) = P_i H_i \left[{H_i}^T P_i H_i + R_i \right]^{-1}$, it can be deduced that:

$$0 < \eta_i H_i(K)^T K_i(K) < 2 \qquad (26)$$

A possible choice for a candidate Lyapunov function form, considering the NAO error $e_i(K)$, can be defined as follows:

$$V(K) = \frac{1}{2} e_i(K)^2 \qquad (27)$$

The variation of $V(k)$ can be determined using the following expression:

$$\Delta V(K) = V(K+1) - V(K) = \Delta e_i(k) \left(e_i(k) + \frac{1}{2} e_i(K) \right) \qquad (28)$$

The variation of the NAO estimation error, denoted as $\Delta e_i(k)$, can be approximated using the following expression:

$e_i(K) = -\left(\frac{\partial e_i(K)}{\partial \theta_i(K)}\right)^T \Delta\theta_i(K) = -\eta_i H_i(K)^T K_i(K) e_i(K)$ As a result, $\Delta V(K)$ can be represented as:

$$\Delta V(K) = \Delta e_i(K) \left(e_i(K) + \frac{1}{2} \Delta e_i(K) \right) = -\eta_i H_i(K)^T K_i \left(1 - \frac{1}{2} \eta_i H_i(K)^T K_i \right) e_i(K)^2 \qquad (29)$$

Given that the inequality in Eq. 23 is satisfied, and with reference to Eqs. 26 and 29, it follows that $\Delta V(K) < 0$. As a result, the weight adjustment in the EKF will converge.

VI. CONTROLLER DESIGN PROCESS

In this method, the controller design process is segmented into two primary stages, each involving its own distinct control loop, as shown in Fig. 8.

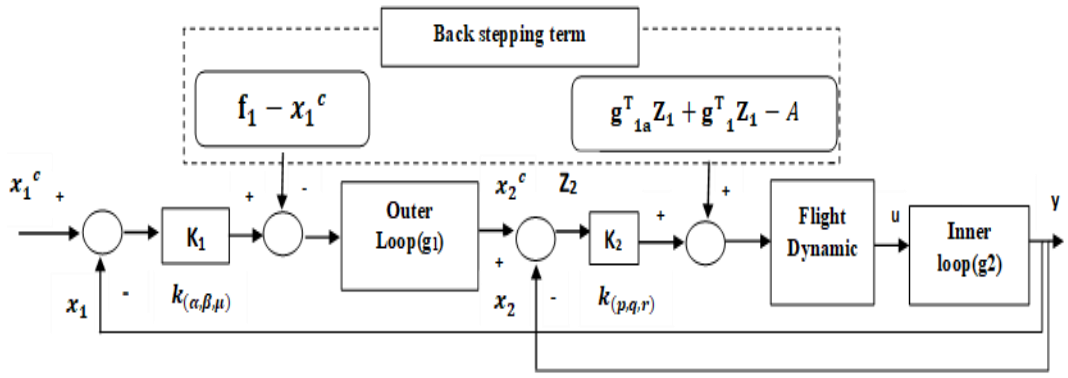

Fig. 8. Controller Overview Using the Back-Stepping Approach

In the external control, slower dynamics are managed. This encompasses parameters like the angle of attack (α),the sideslip angle(β), and the rotation around The direction of the velocity(μ). In contrast, the inner loop focuses on the faster dynamics, specifically the angular rates (p, q, r). The state variables x_1 and x_2 are defined as follows: $x_1 = [\alpha, \beta, \mu]^T$ & $x_2 = [p, q, r]^T$. The control inputs are represented as $u = [\delta_e, \delta_a, \delta_r]^T$. To implement the back-stepping design method effectively, the state variables are redefined in terms of x_1, x_2, and u, as Eq. (30).

$$\begin{cases} \dot{x}_1 = f_1(\alpha, \beta) + g_1(\alpha, \beta, \gamma, \mu) x_2 + g_1(\alpha, \beta) x_2 + h_1(\alpha, \beta) u \\ \dot{x}_2 = f_2(\alpha, \beta, p, q, r) + g_2(\alpha, \beta) u \end{cases} \qquad (30)$$

In the above equations, the parameters f_1, f_2, g_1, g_2 are defined as Eq. (31) as referenced by [20,24].

$$f_1 = \begin{bmatrix} f_\beta(x) \\ f_\alpha(x) \\ f_\mu(x) \end{bmatrix} = \begin{bmatrix} \frac{1}{MV} Y\cos\beta + \frac{1}{MV}[Mg\sin\gamma\sin\mu - T\sin\beta\cos\alpha] \\ \frac{-L}{MV\cos\beta} + \frac{1}{MV\cos\beta}[Mg\cos\gamma\cos\mu - T\sin\alpha] \\ -\frac{g}{V}\tan\beta\cos\mu\cos\gamma + \frac{\tan\gamma}{MV}\left((L+T\sin\alpha)[\sin\mu + \tan\beta] + Y\cos\mu\cos\beta\right) \end{bmatrix}$$

$$g_1(x)=\begin{bmatrix}\sin\alpha & 0 & -\cos\alpha\\ -\tan\beta\cos\alpha & 1 & -\tan\beta\sin\alpha\\ \frac{\cos\alpha}{\cos\beta} & 0 & \frac{\sin\alpha}{\cos\beta}\end{bmatrix} \;\&\; g_2(x)=\begin{bmatrix}L_{\delta_A} & 0 & L_{\delta_R}\\ 0 & M_{\delta_E} & 0\\ N_{\delta_A} & 0 & N_{\delta_R}\end{bmatrix} \qquad (31)$$

$$f_2=\begin{bmatrix}f_p(x)\\ f_q(x)\\ f_r(x)\end{bmatrix}=\begin{bmatrix}\frac{(I_{xz}I_x-I_{xz}I_y+I_{xz}I_z)pq+[(I_zI_y-I^2{}_z)-I^2_{xz}]qr}{I_xI_z-I^2_{xz}}+\frac{I_{xz}\hat{n}_{aero}+I_z\hat{l}_{aero}}{I_xI_z-I^2_{xz}}\\ \left[\hat{m}_{aero}+prI_z-prI_x+I_{xz}r^2-I_{xz}p^2\right]/I_y\\ \frac{I_{xz}\hat{l}_{aero}+I_x\hat{n}_{aero}}{I_xI_z-I^2_{xz}}+\frac{[I_x{}^2-I_xI_y)+I^2_{xz}]pq-I_{xz}(I_xqr-I_yqr+I_zqr)}{I_xI_z-I^2_{xz}}\end{bmatrix}$$

The subsequent assumptions are considered throughout the development and evaluation phases of the backward design method:

Assumption 7: The desired trajectories $x_1^c=[\alpha^c,\beta^c,\mu^c]$ are limited. $\|[x_1^c,\dot{x}_1^c,\ddot{x}_1^c\| \le c_d$

which $c_d \in R$ represents a known positive constant, while$\|.\|$ the soft sign function for the two vectors can be defined as:matrices $\dot{x}_1^c$ and $\ddot{x}_1^c$ is the first and second derivative of the input command signal.

Assumption 8: Speed and dynamic pressure change according to flight height. $\dot{V}\neq 0,\dot{\bar{q}}\neq 0$

Assumption 9: The deviation of the control surfaces has no effect on the aerodynamic force: $h_1(\alpha,\beta)=0$

The error of state variables and control input u is defined as follows:

$$\begin{cases} z_1 = x_1 - x_1^c \& z_2 = x_2 - x_2^c \\ x_2^c = g_1^{-1}[-k_1 z_1 - f_1 + \dot{x}_1^c] \\ u = g_2^{-1}[-k_2 z_2 - g_1^T z_1 - g_1^T z_1 - A] \\ A = f_2 + f_2 x_2 - g_1^{-1}[k_1 \dot{x}_1^c + \ddot{x}_1^c] \end{cases} \qquad (32)$$

The proposed methodology involves an ASTO for disturbance elimination and attenuation, combined with a neural-adaptive network and Kalman filter for error detection. Fig. 9 illustrates the overall schematic of the sensor error detection and disturbance reduction methodology.

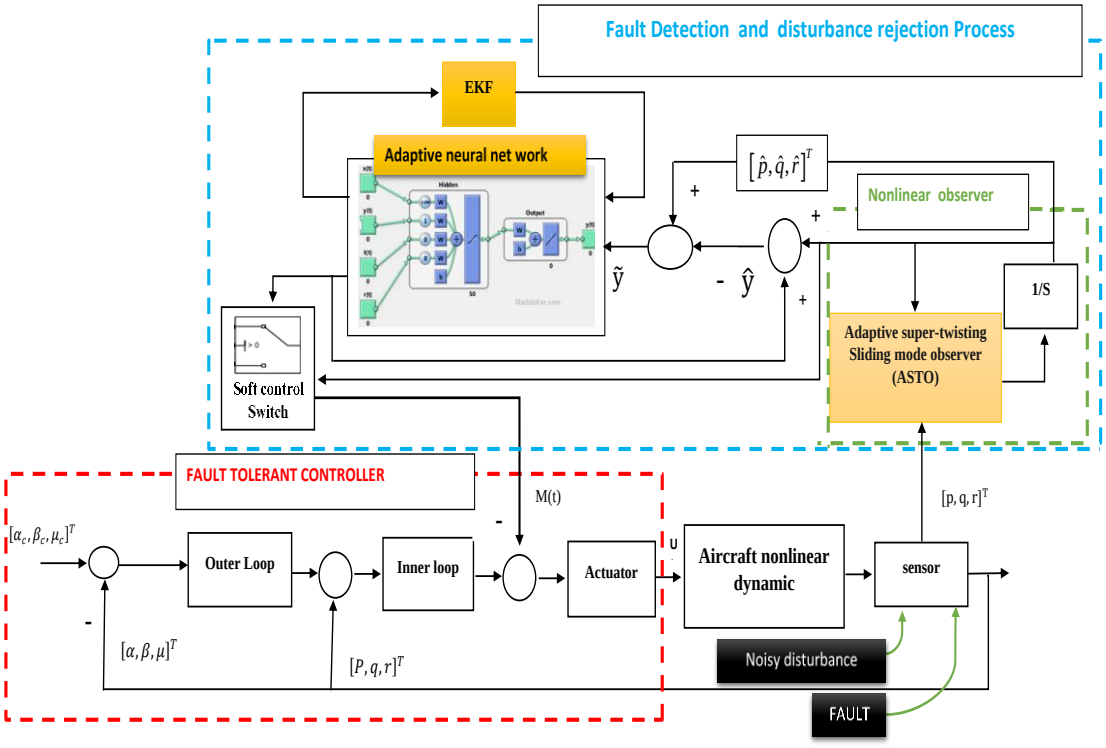

Fig. 9. Overall process of noise removal and error detection

VII. DESIGNING A FAULT-TOLERANT CONTROLLER

After error identification and detection, the next step is designing a controller to mitigate the errors' effects. Various methods, including LQR, robust control, adaptive control techniques, and sliding mode-based approaches, have been proposed. This study employs an adaptive approach to adapt the system to error-inclusive conditions. This research focuses solely on sensor errors. The state equations for the nonlinear system incorporating these errors are provided in eq. (33) by ref. [24].

$$\begin{cases} \dot{x} = f(x,u) \\ y = Cx(t) + F_s f_s \end{cases} \quad (33)$$

Which f_s indicates the unknown input (error) of the sensor. The derivatives of the states (p,q,r) in eq. (34).

$$\begin{bmatrix} \dot{p} \\ \dot{q} \\ \dot{r} \end{bmatrix} = \begin{bmatrix} \dot{p}_c + K_p(p_c - p) \\ \dot{q}_c + K_q(q_c - q) \\ \dot{r}_c + K_r(r_c - r) \end{bmatrix} \quad (34)$$

The flight control system is streamlined by omitting the first-order derivatives of the input command as shown in equation (34). Sensor inaccuracies are included in the feedback process for controlling the fighter aircraft, roll, pitch, & yaw, leading to an overall summation. The total sensor error is defined in equation (35).

$$\begin{aligned} p_F &= p + F_{s_1} f_s \rightarrow F_{s_1} f_s = \hat{p} \\ q_F &= q + F_{s_2} f_s \rightarrow F_{s_2} f_s = \hat{q} \\ r_F &= r + F_{s_3} f \rightarrow F_{s_3} f_s = \hat{r} \end{aligned} \quad (35)$$

Where p_F, q_F, r_F the measured values by the sensors are accompanied by errors, and the true error-free values are represented by (p,q,r) and f_s the unknown input is the sensor error, and(F_{s_1},F_{s_2},F_{s_3}) represent the error magnitude. It should be noted that $\hat{p}, \hat{q}, \hat{r}$ are estimated by the adaptive neural observer. In equations (30) to (32), instead of the fast state equations (p,q,r), the values (p_F,q_F,r_F) with errors should be substituted. The new system input, comprising both the nominal and adaptive components designed to mitigate error effects, is defined by eq. (36).

$$u_{new} = u + u_{ad} \quad (36)$$

The vector u is defined in equation (32). By algebraic manipulations on the equation (30) the adaptive control input is derived eq. (37) as referenced by [24] .

$$u_{ad} = g_2^{-1}\left(\begin{bmatrix} k_p(\hat{p}) \\ k_q(\hat{q}) \\ k_r(\hat{r}) \end{bmatrix} + \begin{bmatrix} f_{\hat{p}}(x) \\ f_{\hat{q}}(x) \\ f_{\hat{r}}(x) \end{bmatrix} - \begin{bmatrix} \alpha_c \sin\alpha - \alpha \sin\alpha - cos\alpha\, tg\beta(\beta_c - \beta) + \frac{cos\,\alpha}{cos\,\beta}(\mu_c - \mu) \\ \beta_c - \beta \\ -cos\alpha(\alpha_c - \alpha) - tg\beta \sin\alpha + \frac{sin\,\alpha}{cos\,\beta}(\mu_c - \mu) \end{bmatrix} - g_1^{-1}\begin{bmatrix} \dot{\alpha}_c k_\alpha + \ddot{\alpha}_c \\ \dot{\beta}_c k_\beta + \ddot{\beta}_c \\ \dot{\mu}_c k_\mu + \ddot{\mu}_c \end{bmatrix}\right) \quad (37)$$

VIII. SOFT CONTROL SWITCH DESIGN

To achieve seamless switching during faults or sensor failures, the control switch is governed by the matrix M(t), which reflects the output of the neural network. When there are no faults, M(t), is zero, meaning the angular velocity is directly based on the actual sensor data. However, if a fault occurs such as a sensor failure or loss of data the system smoothly transitions to the estimated angular velocity, computed by the Adaptive Super-Twisting Observer(ASTo).

This smooth transition is facilitated by soft switching techniques, which use sigmoid-based weighting functions to avoid abrupt changes. These methods are especially useful in high-stability applications like flight control systems that require fault tolerance. Key parameters such as the softness coefficient (α) and error threshold (τ) are crucial in fine-tuning the transition, ensuring the system reacts efficiently to faults, disturbances, or sensor unavailability, while minimizing control time and energy consumption [25].The weighting function for smooth transitions is based on a sigmoid function by the following equation.

$$w\left(\begin{bmatrix} p \\ q \\ r \end{bmatrix}\right) = 1/(1 + e^{-\alpha\left(\tau - e\left(\begin{bmatrix} p \\ q \\ r \end{bmatrix} - \begin{bmatrix} \hat{p} \\ \hat{q} \\ \hat{r} \end{bmatrix}\right)\right)}) \quad (38)$$

In equation (38) α Smoothness factor for switching term and τ Error threshold for switching to estimated data. Final Switched Outputs in eq. (39)by reference[26].

$$\begin{bmatrix} p \\ q \\ r \end{bmatrix}_{m(t)} = w\left(\begin{bmatrix} p \\ q \\ r \end{bmatrix}\right) \times \begin{bmatrix} p \\ q \\ r \end{bmatrix}_{real} + (1-w) \times \begin{bmatrix} \hat{p} \\ \hat{q} \\ \hat{r} \end{bmatrix} \quad (39)$$

In conclusion, by introducing the control switch controlled by the M(t), matrix and employing soft switching with sigmoid-based weighting functions, the system achieves seamless transitions between actual and estimated angular velocity. This method enhances overall performance, particularly in fault detection and tolerance, resulting in improved stability and reduced control time and energy usage. The coefficients are carefully selected through empirical tuning to achieve the best possible switching performance, minimizing errors while maximizing efficiency. By defining the control switch, if the matrix M(t), of the output of the neural network is zero according to Fig. 7 and there is no fault in the system, the angular velocity value is based on the real angular velocity, and if a fault occurs and the output of the angular velocity sensor has a problem or is unavailable instead, it takes advantage of the estimated angular velocity by the super twisting algorithm, which consumes less control time and energy.

IX. FINDINGS FROM THE SIMULATION

This part assesses how well the designed controller corrects errors from the three sensors (p, q, r).Challenging simulation scenarios are created by introducing soft, abrupt, and transient sensor errors, which are identified and separated using an adaptive neural observer. The initial parameters of the observers are obtained from Table (3).

Table 3. The initial values for the three EKF estimators for p, q, and r

R_0	θ_0	P_0	η	Initial values of Observer
0.00002	$\theta_0 = [2; 0.3; 1]$	$40 \times I_{3\times3}$	0.4	(estimation error **p**)
0.00002	$\theta_0 = [1.9; 0.5; 0.5]$	$1 \times I_{3\times3}$	0.4	(estimation error **q**)
0.00002	$\theta_0 = [1.5; 1.5; 1]$	$1 \times I_{3\times3}$	0.4	(estimation error **r**)

The desired values for (α, β, μ) the following selections were made $\{\beta = 0^{\circ} t \geq 0; \alpha = 5°\&\mu = 10°\ t \geq 0.5\}$

Here, the effects of a transient error are introduced in the yaw sensor for three scenarios: In Fig 10.

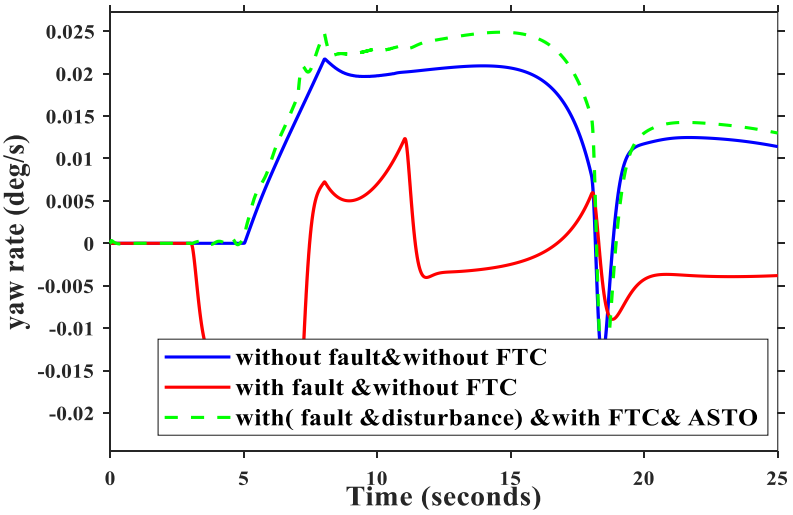

Fig. 10 .Variations in yaw rate over time.

Figure (11) shows the variations in rudder control and Figure (12) shows the variations in aileron control surface.

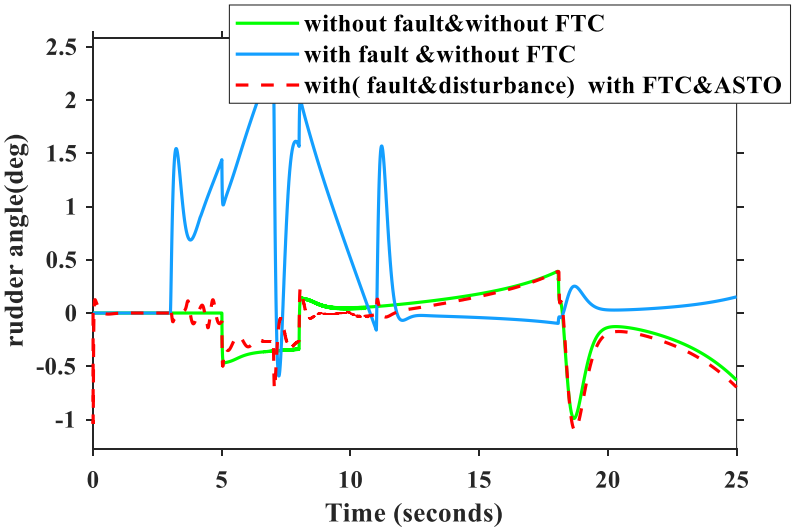

Fig. 11. rudder control surface deflections over time under three conditions: (1) in the absence of errors, disturbances,and FTC; (2) with a transient error in the r sensor but without applying FTC and ASTO; and (3) with a transient error while implementing FTC and ASTO.

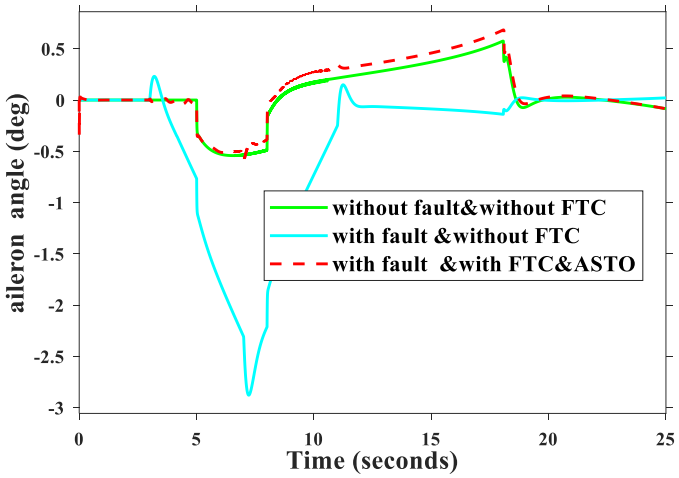

Fig. 12. Aileron control surface deflections over time under three conditions: (1) in the absence of errors, disturbances, and FTC; (2) with a transient error in the r sensor but without applying FTC and ASTO; and (3) with a transient error while implementing FTC and ASTO.

The designed controller's effectiveness in compensating for errors during maneuvering flight is demonstrated. Errors in all three sensors are assumed to occur in the third second.

Table 4. The control commands for α, β, and μ

Time(sec)	α_d	β_d	$\dot{\mu}_d$
$t < 2 \geq 0$	0	0	0
$t < 5 \geq 2$	10	0	0
$t < 8 \geq 5$	10	0	2
$t < 18 \geq 8$	0	0	0
$t < 25 \geq 18$	0	0	0

For assessing the system's tolerance threshold, reference signal tracking, and stability, Gaussian white noise with a signal-to-noise ratio (SNR) between 20 and 40 dB is commonly applied. This noise simulates environmental disturbances affecting aircraft sensors, characterized by a zero mean and a specified variance. The application of this noise is illustrated in Figure 13.

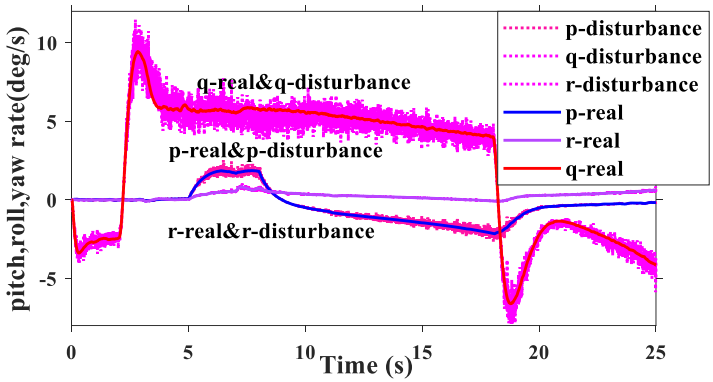

Fig. 13. Disturbance applied to the aircraft's angular velocity sensor as white Gaussian noise.

In Fig. (14) the simulation results for tracking reference signal x_1^c. with Fault-Tolerant Backstepping Controller and Without Adaptive Super-Twisting disturbance rejection are shown.

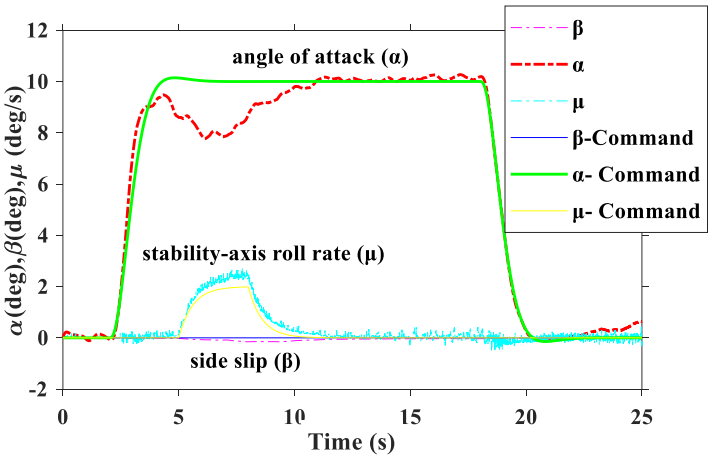

Fig. 14 .Reference model with FTC & without ASTO disturbance rejection

In Fig. (15) the simulation results for tracking reference signal x_1^c. with Fault-Tolerant Backstepping Controller and With Adaptive Super-Twisting disturbance rejection are shown.

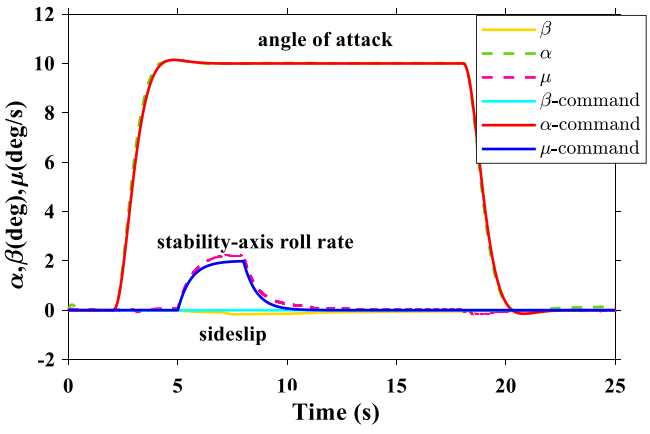

Fig. 15. Reference model with FTC & ASTO disturbance rejection.

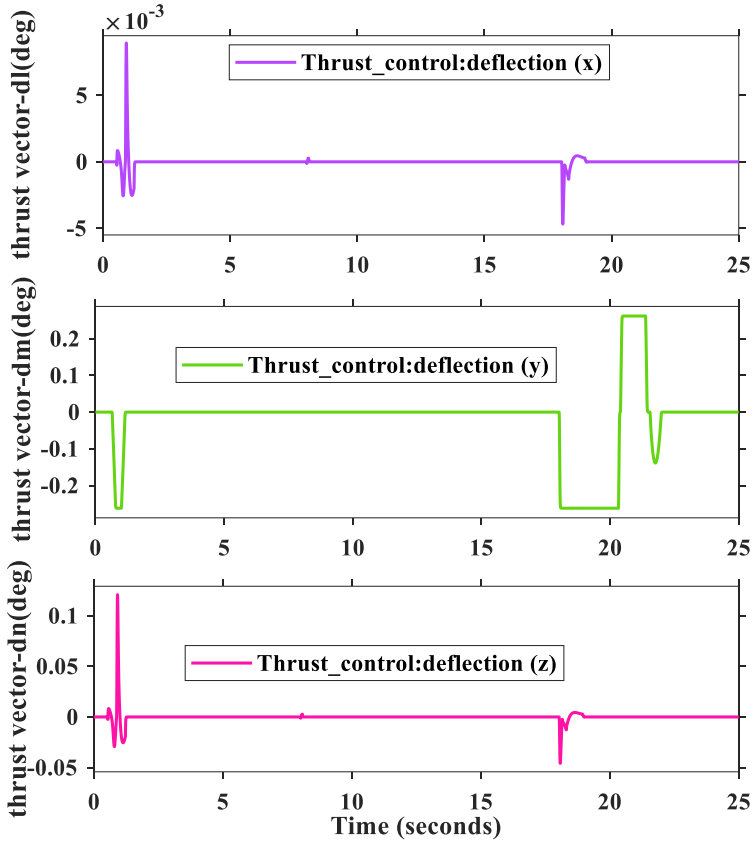

Fig. 16. Thrust vector variation in three directions at high angles of attack in the presence of sensor fault and disturbance.

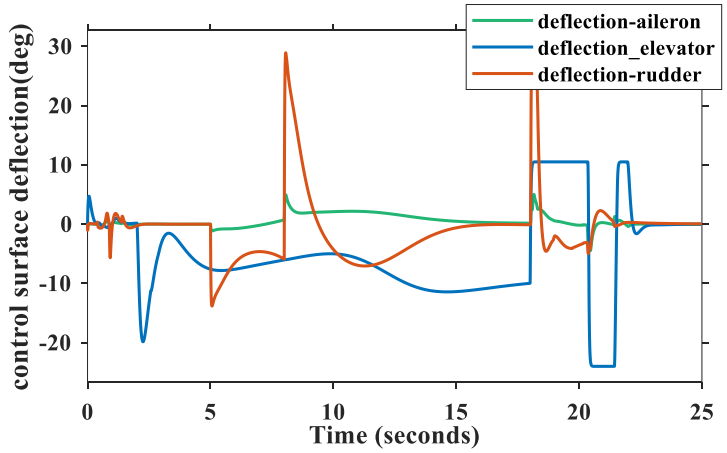

Fig. 17. Variation of aerodynamic control surfaces under elevated angles of attack in the presence of sensor faults and disturbances

X. ALGORITHM TOLERANCE AT HIGH ANGLE OF ATTACK

Grounded in the reviewed literature and as highlighted in references [20], achieving a fault-tolerant control (FTC) system under high AoA (Angle of Attack) situations remains a substantial challenge. While recent studies have proposed fault-tolerant sensor algorithms for these scenarios, they often exhibit limited robustness in the presence of concurrent sensor faults and severe noise, emphasizing the need for more resilient control strategies.The standard F-18 aircraft can achieve angles of attack exceeding 40°; however, at this threshold, conventional roll

control becomes nearly ineffective. To address this limitation, the High Alpha Research Vehicle (HARV) was introduced, employing thrust vectoring to restore maneuverability in extreme flight conditions. Given the pronounced instability associated with 40° AoA, This threshold acts as a crucial reference point for evaluating the performance of fault-tolerant algorithms. While thrust vectoring systems theoretically enable controllability at AoAs of up to 70°, the 40° threshold remains a particularly challenging reference point for assessing control robustness [27-28]. Although conventional operations typically limit AoA to around 26° for safety, experimental investigations have ventured beyond this range to explore post-stall dynamics, revealing challenges such as flow separation and pronounced nonlinear aerodynamic effects [29].To mitigate these complexities, adaptive control strategies have been extensively explored, demonstrating substantial improvements in stability and maneuverability. Notably, Sadati's research has illustrated the effectiveness of advanced control enhancements under high AoA conditions. Nevertheless, recent findings indicate that existing fault-tolerant algorithms often fail to maintain robustness when exposed to simultaneous sensor faults and severe noise. This persistent challenge underscores the necessity for further advancements in adaptive fault-tolerant control systems [20].

A key contribution of this study is its ability to maintain accurate and stable control at high AoAs, even in the presence of sensor faults and disturbances. Thrust vectoring has been incorporated into the dynamic equations to enhance maneuverability and tracking at high angles of attack This paper presents a comprehensive comparative performance analysis of two advanced FTC algorithms under these challenging conditions. The first algorithm, referred to as Algorithm 1, integrates FTC with Backstepping Control and a Super-Twisting Observer (STO). The second algorithm, Algorithm 2, employs FTC with Backstepping Control and an Adaptive Super-Twisting Observer (ASTO). The comparative evaluation is carried out using essential tracking performance indicators, such as Root Mean Square (RMS) Error, Maximum Error, Integral Absolute Error (IAE), and Integral Squared Error (ISE), with results detailed in Table 5. Additionally, Table 6 presents performance improvements, while Table 7 provides a comparative analysis of algorithm tolerance for ramp input scenarios.

Table .5. Comparative Performance Analysis of FTC Algorithms.

Performance Metric	Algorithm 1 (FTC +STO)	Algorithm 2 (FTC +ASTO)
RMS Error (°)	4.23575	3.423
Max Error (°)	10.85630	10.86364
IAE (°·s)	16668.70427	8614.7
ISE (^{o2}·s)	112152.66855	92894.1

Table .6. Performance Improvement of Algorithm 2 over Algorithm 1

Improvement Metric	Percentage Improvement
RMS Error Improvement	13.27%
IAE Improvement	48.3%
ISE Improvement	17.2%
Chattering index	5.7%

Table 7. Algorithm tolerance comparison for ramp input.

Simulation	Fault	Disturbance	Disturbance + Fault
Adaptive neural network + Backstepping control	0.2°/s	0.12°/s	0.11°/s
Adaptive neural network +STA+Backstepping control	0.26°/s	0.4°/s	0.2°/s
Adaptive neural network + ASTO + Backstepping control	0.33°/s	0.48°/s	0.27°/s

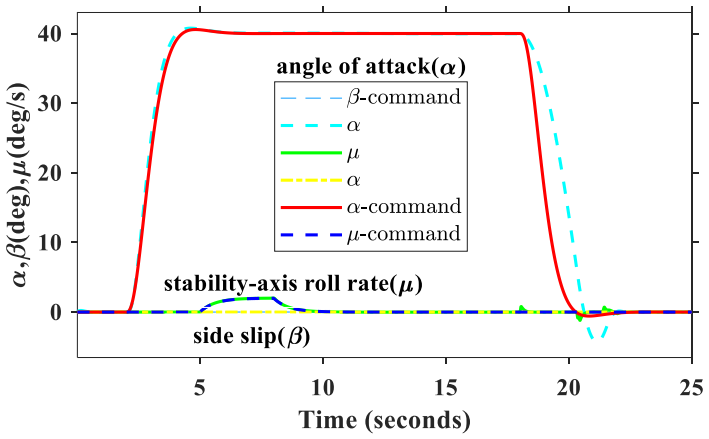

Fig. 18. High-angle-of-attack reference tracking under sensor faults and disturbance by FTC+ASTO

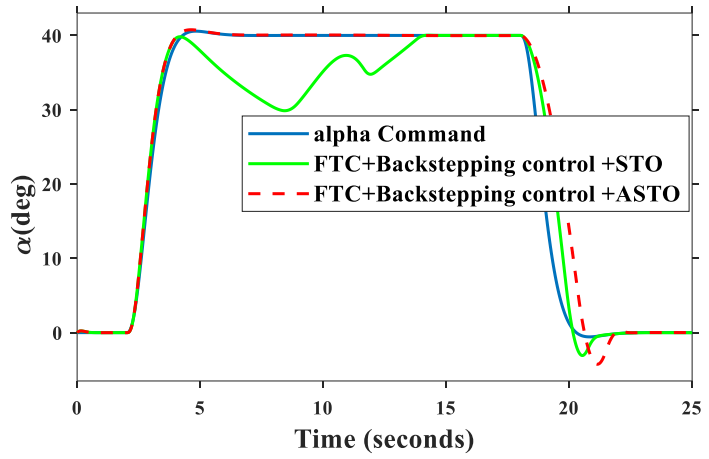

Fig. 19. Reference signal tracking at high angles of attack under sensor faults and severe noise disturbances by two algoritm ASTO and STO

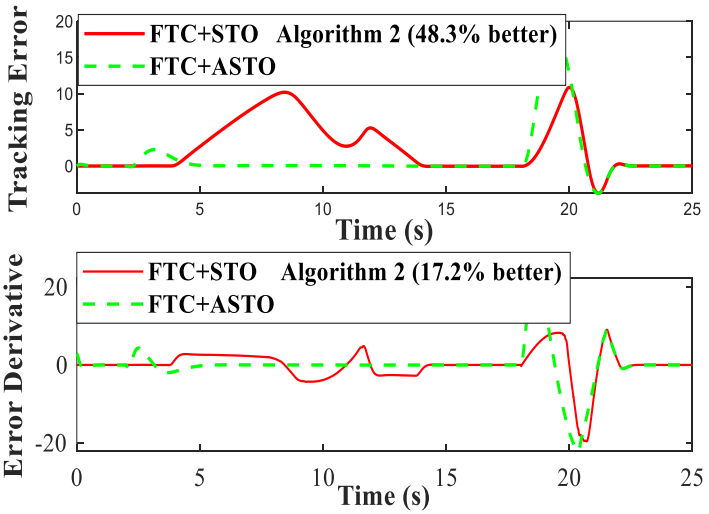

Fig. 20. High-angle-of-attack reference tracking under sensor faults and severe noise disturbances:

A comparative evaluation of tracking error and the rate of change of tracking error.

Figure 18 illustrates how the FTC+ASTO approach performs effectively in demanding operational scenarios, where faults and disturbances were applied to the angular velocity sensor r at a high angle of attack. The algorithm exhibited remarkable stability and achieved accurate tracking. To further evaluate its robustness, a comparative analysis was conducted under the same operational scenario using the FTC+STO algorithm, as depicted in Fig. 19, Due to its lack of adaptivity and inability to adjust its coefficients in response to disturbances, the FTC+STO algorithm exhibited significant performance degradation, resulting in poor tracking capability. In contrast, the FTC+ASTO algorithm effectively mitigated the impact of disturbances and maintained superior tracking performance. Specifically, as illustrated in Figure 20, the FTC+ASTO algorithm achieved a 48.3% reduction in tracking error and a 17.2% decrease in the rate of error change, demonstrating its exceptional resilience and adaptability.

XI. CONCLUSIONS

This study introduces a novel approach to fault-tolerant flight control, significantly enhancing aircraft stability and reliability in the presence of sensor faults and disturbances. By integrating the adaptive Super-Twisting Algorithm (ASTO) with an Adaptive Neural Observer-Extended Kalman Filter (ANO-EKF) and a Backstepping-based control strategy, the proposed system achieves superior disturbance rejection and adaptability to unknown perturbations.A key breakthrough of this research is its ability to ensure accurate control at increased angles of attack (40°), a regime where conventional methods struggle. The results demonstrate clear performance gains, with RMS error reduced by 13.27%, Integral Absolute Error (IAE) improved by 48.3. %, and Integral Squared Error (ISE) reduced by 17.2%, Chattering index reduced by 5.7% highlighting the effectiveness of this approach over traditional techniques.Furthermore, by addressing control signal discontinuities and optimizing controller and observer coefficients, this method ensures smoother control actions, more accurate state estimation, and enhanced robustness. The proposed framework sets a new benchmark for resilient aerospace systems, marking a significant step forward in high-performance flight control under real-world operational constraints.

ACKNOWLEDGEMENTS:

The authors sincerely appreciate the dedication and commitment of the editor and associate editor in evaluating and refining this work. They also extend their gratitude to the anonymous reviewers for their thoughtful insights and valuable recommendations, which have greatly contributed to enhancing the overall quality of this research.

Conflict of Interest : The authors affirm that no conflicts of interest are associated with this study.

Funding: The authors received no financial support for this research.

APPENDIXES:

The following model was used for the aerodynamic force coefficients and moments in this article These references are based on [30].

Drag coefficient:

$$C_D = \begin{cases} 0.0013\alpha^2 - 0.00438\alpha + 0.0297 & -5 \le \alpha \le 20 \\ -0.0000348\alpha^2 + 0.0473\alpha - 0.45846 & 20.0 \le \alpha \le 40.0 \end{cases} \quad (40)$$

the coefficient representing the lateral force:

$$C_Y = \frac{\delta_r}{30}(-0.00265\alpha + 0.141) + \frac{\delta_a}{25}(-0.00227\alpha + 0.039) - 0.0186\beta \quad (41)$$

Coefficient of Lift force:

$$C_L = \begin{cases} 0.0751\alpha - 0.0309 + 0.0144\delta_e & -5.0 \le \alpha \le 10.0 \\ -0.00148\alpha^2 + 0.569 + 0.106\alpha + 0.0144\delta_e & 10.0 \le \alpha \le 40.0 \end{cases} \quad (42)$$

Roll moment coefficient:

$$C_l = -0.0315p + 0.0126r - \frac{\delta_r}{30}(0.000351\alpha - 0.0124) + \frac{\delta_a}{25}(0.00121\alpha - 0.0628) + C_l(\alpha,\beta) \quad (43)$$

$$C_{l_{(\alpha,\beta)}} = \begin{cases} (-0.00092 - 0.00012\alpha)\beta & -5.0 \le \alpha \le 15.0 \\ (-0.006 + 0.00022\alpha)\beta & 15.0 \le \alpha \le 25.0 \end{cases} \quad (44)$$

coefficient of rotational force:

$$C_M = 0.0166 - 0.00437\alpha - 0.0196\delta_e - 0.123q \quad (45)$$

coefficient of yawing moment:

$$C_n = \frac{\delta_r}{30}(0.000804\alpha - 0.0474) + C_n(\alpha,\beta) + \frac{\delta_a}{25}(0.000213\alpha + 0.00128) - -0.0142r \quad (46)$$

$$C_n(\alpha,\beta) = \begin{cases} 0.00125\beta & -5.0 \le \alpha \le 10.0 \\ (0.00342 - 0.00022\alpha)\beta & 10.0 \le \alpha \le 25.0 \\ -0.00201\beta & 25.0 \le \alpha \le 35.0 \end{cases} \quad (47)$$

In equations (40) to (48), all angles and deflections of the control surfaces are given in degrees, while the angular velocities are specified in radians. The maximum thrust in the longitudinal direction, depending on the Mach number, can be expressed as follows [31][32].

$$T_{x_{MAX}}(M) = 5500\, sin(\,2.1(M - 0.7)) + 24000 \quad (48)$$

Through interpolation between different throttle settings, thrust can be expressed in terms of both throttle setting and Mach number, as demonstrated here:

$$\mathrm{T_x}(\mathrm{M}, \mathrm{t_h}) = \mathrm{T_x}\max(\,\mathrm{M})\left[\frac{\mathrm{t_h} - 30^\circ}{100^\circ}\right] \quad (49)$$

The constant values and information related to the F-18/A aircraft are provided in Table (P-1), and the range of motion and rotation rates of the control surfaces are given in Table (P-2).

Table P-1 F-18/A aircraft information

$S = 400ft^2$	$m = 1036slug$
$b = 37.42$ft	$I_x = 23000slugft^2$
c=11.52	$I_y = 151293slugft^2$
$I_{xz} = -2131.8slugft^2$	$I_z = 169945slugft^2$

Table P-2 Control surface deflection ranges and rotation rates, along with thrust vectoring capabilities of the F/A-18.

$\delta_e(t) \in [-24\,\mathrm{deg}, +10.5\mathrm{deg}]$	$\lvert\dot{\delta}_e(t)\rvert \le 40$ deg/s
$\delta_r(t) \in [-30\,\mathrm{deg}, +30\mathrm{deg}]$	$\lvert\dot{\delta}_r(t)\rvert \le 56$ deg/s
$\delta_a(t) \in [-25\,\mathrm{deg}, +25\mathrm{deg}]$	$\lvert\dot{\delta}_a(t)\rvert \le 100$ deg/s
$\eta(t) \in [0, +1.0]$	$\lvert\dot{\eta}(t)\rvert \le 0.55$ deg/s

XII. References

[1] H. K. Khalil, Nonlinear Systems, 3rd ed., Upper Saddle River, NJ: Prentice Hall, 2002.

[2] Z. Guo, J. Guo, J. Zhou, and J. Chang, "Robust tracking for hypersonic reentry vehicles via disturbance estimation-triggered control," IEEE Trans. Aerosp. Electron. Syst., vol. 56, no. 2, pp. 1279-1289, 2020.

[3] X. Wu and X. Mu, "New design on distributed event-based sliding mode controller for disturbed second-order multi-agent systems," IEEE Trans. Autom. Control, vol. 67, no. 5, pp. 2590-2596, 2021.

[4] J. Liu, H. An, Y. Gao, C. Wang, and L. Wu, "Adaptive control of hypersonic flight vehicles with limited angle-of-attack," IEEE/ASME Trans. Mechatronics, vol. 23, no. 2, pp. 883-894, 2018.

[5] R. Sankar, B. Bandyopadhyay, and H. Arya, "Robust control and state estimation of the micro aerial vehicle using sliding mode technique," in Proc. 54th IEEE Conf. Decis. Control, 2015, pp. 1-6.

[6] 1] J. Karimi, S. Mohammadnejad, and A. Babai, "A new two-step robust strategy for estimating the line-of-sight rate of optical seekers having time delay," *J. Braz. Soc. Mech. Sci. Eng*., vol. 47, p. 145, 2025.

[7] X. Qi, C. Li, Y. Jing, and H. Ma, "Super twisting observer-based arbitrary convergence time sliding mode control for uncertain systems," Int. J. Control Autom. Syst., 2024, pp. 1-9.

[8] S. Balajiwale, H. Arya, and A. Joshi, "Longitudinal controller for hand launched MAV based on supertwisting algorithm," in Proc. AIAA Guidance, Navigation, and Control Conf., 2017, pp. 1-6.

[9] Z. Gao, C. Cecati, and S. X. Ding, "A survey of fault diagnosis and fault-tolerant techniques-Part I: Fault diagnosis with model-based and signal-based approaches," IEEE Trans. Ind. Electron., vol. 62, no. 6, pp. 3757-3767, 2015.

[10] M. A. Gomaa and T. N. Vijaykumar, "Opportunistic transient-fault detection," in Proc. 32nd Int. Symp. Comput. Archit. (ISCA), 2005, pp. 172-183.

[11] A. A. Pashilkar and N. Sundararajan, "A fault-tolerant neural aided controller for aircraft auto-landing," Aerosp. Sci. Technol., vol. 10, no. 1, pp. 49-61, 2006.

[12] M. Di Bernardo, U. Montanaro, and S. Santini, "Novel hybrid MRAC-LQ control schemes: synthesis, analysis and applications," Int. J. Control, vol. 81, no. 6, pp. 940-961, 2008.

[13] A. Guven and C. Hajiyev, "Sensor fault detection, isolation, and accommodation applied to B-747," in Solutions for Maintenance Repair and Overhaul, ISATECH 2021, Sustainable Aviation, Springer, Cham, 2024, pp. 379-386.

[14] D. Ye, Q. Y. Fan, G. H. Yang, and H. Wang, "Robust H∞ fault-tolerant control for linear systems with fast adaptive fault estimation," IFAC Proc. Vol., vol. 47, no. 3, pp. 6753-6757, 2014.

[15] J. Hu, Y. Sha, and J. Yao, "Dual neural networks based active fault-tolerant control for electromechanical systems with actuator and sensor failure," Mech. Syst. Signal Process., vol. 182, p. 109558, 2023.

[16] B. Yu, Y. Zhang, and Y. Qu, "MPC-based FTC with FDD against actuator faults of UAVs," in Proc. 15th Int. Conf. Control, Autom. Syst. (ICCAS), 2015.

[17] X. Qi, C. Li, Y. Jing, et al., "Super twisting observer-based arbitrary convergence time sliding mode control for uncertain systems," Int. J. Control Autom. Syst., vol. 22, pp. 883-891, 2024.

[18] R. C. Nelson, Flight Stability and Automatic Control, vol. 2, New York: WCB/McGraw Hill, 1998.

[19] B. L. Stevens, F. L. Lewis, and F. Al-Sunni, "Aircraft flight controls design using output feedback," J. Guidance, Control, Dyn., vol. 15, no. 1, pp. 238-246, 1992.

[20] S. H. Sadati, M. S. Parvar, M. B. Menhaj, et al., "Backstepping controller design using neural networks for a fighter aircraft," Eur. J. Control, vol. 13, no. 5, pp. 516-526, 2007.

[21] A. R. Babaei, M. Malekzadeh, and D. Madhkhan, "Adaptive super-twisting sliding mode control of 6-DOF nonlinear and uncertain air vehicle," Aerosp. Sci. Technol., vol. 84, pp. 361-374, 2019.

[22] Q. Wu and M. Saif, "Neural adaptive observer based fault detection and identification for satellite attitude control systems," in Proc. Am. Control Conf., 2005, pp. 1054-1059.

[23] K. Funahashi and Y. Nakamura, "Approximation of dynamical systems by continuous time recurrent neural networks," Neural Netw., vol. 6, no. 6, pp. 801-806, 1993.

[24] A. Abaspour, S. H. Sadati, and M. Sadeghi, "Nonlinear optimized adaptive trajectory control of helicopter," Control Theory Technol., vol. 13, pp. 297-310, 2015.

[25] J. Wan, B. He, Y. Shen, W. Liu, X. Ding, and S. Gao, "Heading multi-mode control based on soft-switching for autonomous underwater vehicle," Ocean Engineering, vol. 164, pp. 672-682, 2018.

[26] Y. Lu, X. Huang, Y. Huang, and D. Liu, "Sigmoid function model for a PFM power electronic converter," IEEE Transactions on Power Electronics, vol. 35, no. 4, pp. 4233-4241, 2019.

[27] Meyn L, Lanser W, James K. Full-scale high angle-of-attack tests of an F/A-18. In: Proceedings of the 10th Applied Aerodynamics Conference; 1992.

[28] Regenie V, Gatlin D, Kempel R, Matheny N. The F-18 High Alpha Research Vehicle—A high-angle-of-attack testbed aircraft. In: Proceedings of the 6th AIAA Biennial Flight Test Conference; 1992. p. 4121.

[29] Patten WN. The poststall non-linear dynamics and control of an F-18: A preliminary investigation. Hampton Institute, NASA/American Society for Engineering Education; 1988.

[30] Y. Fan, F.H. Lutze, and E.M. Cliff, "Time-optimal lateral maneuvers of an aircraft," J. Guidance, Control, Dyn., vol. 18, no. 5, pp. 1106-1112, 1995.

[31] K.H. Well, B. Faber, and E. Berger, "Optimization of tactical aircraft maneuvers utilizing high angles of attack," J. Guidance, Control, Dyn., vol. 5, no. 2, pp. 131-137, 1982.

[32] E. Hoffman and H. Stalford, "Singular trajectories for time-optimal half-loop maneuvers of a high-alpha fighter aircraft," in Guidance, Navigation and Control Conference 1989, p. 3614, 1989.